Numerical Simulation of Air-He Shock Tube Flow with Equilibrium Air Model

Hua Chen[1]

Department of Information Communication, Leader University, Taiwan, 70970

Chih-Yung Wen[2,*] and Chih-Kai Yang[2]

Institute of Aeronautics and Astronautics, National Cheng Kung University, Taiwan 70100

In this study, a compressible multi-component Navier-Stokes flow solver with real gas effect is developed for studying the high-speed flow in an air-He shock tube. For compressible multi-component flow simulation, a reduced five-equation model in conjunction with HLLC approximate Riemann solver is employed. For the real gas effect, a curve-fitting approximation for equilibrium air constructed from Grabau-type transition functions is adopted. In addition, Baldwin-Lomax turbulence model is used for turbulent flow simulation. In this work, several typical test cases will be demonstrated first. Subsequently, air-He shock tube simulations with the real gas effect will be performed by using parallel computation. Based on the present results, the real gas effect shows significant influence on the temperature behind the reflected shock. In addition, the driver gas contamination and the development of shock bifurcation are presented by flow visualization.

AIAA associate fellow, Corresponding author,
Tel: +886 6 2757575 ext. 63657;Fax:+886 6 2349281;*E-mail address*: cywen@mail.ncku.edu.tw

Nomenclature

c	=	speed of sound
E	=	total energy
e	=	specific internal energy
i	=	index of fluid species
M_s	=	incident shock Mach Numbers
p	=	pressure
P_1	=	initial driven pressure
P_2	=	pressure behind the incident shock
P_4	=	initial driver pressure
P_5	=	pressure behind the reflected shock
P_{41}	=	initial (diaphragm) pressure ratio
Pr	=	Prandtl Number
Re	=	Reynolds Number
T	=	temperature
t	=	time
U	=	velocity vector
u, v	=	velocity components in x and y directions
W	=	$u_s/(u_s - u_2)$

x, y	=	coordinates
x_s	=	shock distance from the diaphragm
X	=	distance of triple point to the end wall
Y	=	height of triple point
α	=	volume fraction
Φ	=	0 for two-dimensional flow; 1 for axisymmetric flow
$\emptyset$	=	angle between the front leg of bifurcation and the wall surface
η	=	$x_s/W\iota_m$
γ	=	specific heat ratio
ι	=	separation distance
ι_m	=	maximum separation distance
μ	=	viscosity coefficient
π	=	mixture reference pressure
θ	=	angle between the oblique shock and the wall surface
ρ	=	density
ρ_0	=	density of gas under standard condition
ζ	=	ι/ι_m
τ	=	shear stress

I. Introduction

Reflected shock tunnels are usually designed for hypersonic flow or high-enthalpy flow researches. Over decades, a number of studies of reflected shock tunnels have been reported on important problems such as the

shock/boundary layer interactions, test time, and driver gas contamination, etc. However, only few studies focused on hypersonic reflected shock tunnels were conducted by using numerical simulations. Although computational fluid dynamics (CFD) has been widely used in many practical applications, numerical simulations of high-speed multi-component flows remain a challenge for CFD. At present, challenges for high-speed multi-component flow simulations include compressible multi-component flow models, robust numerical schemes, real gas effect, chemical reactions, etc. Regarding to these issues, this work aims to develop a numerical approach for compressible multi-component flow simulations with the real gas effect in the shock tube part of a reflected shock tunnel.

For the shock tube studies, one of the most challenges is shock/boundary layer interactions. The first attempt to propose a flow model for reflected shock/boundary layer interaction was by Mark [1]. In his model, the velocity of the reflected shock, bifurcation and shock angle in the bifurcated foot were predicted. However, the height of the bifurcated foot was not predicted in his analyses. Subsequently, Matsuo et al. [2] observed the interaction of the reflected shock and the boundary layer optically by using Schlieren images. A modified flow model of the reflected shock/boundary layer interaction was proposed. By using the new model, the predicted results of the growth rate of the bifurcation and the velocity of the reflected shock were improved in comparison with Mark's model [1]. Weber et al. [3] numerically studied the shock bifurcation in the shock tube. The numerical simulations were implemented by using a data parallel version of flux-corrected transport (FCT) algorithm. All simulations were performed using calorically perfect air and the shock Mach numbers (Ms) were in the range of 2.6 to 10. They investigated the influence of heat transfer, Reynolds number and incident shock strength on the viscous interactions. Besides, it was noted that numerical investigation of the reflected shock/boundary layer interaction provided many detailed shock bifurcation physics. Burtschell et al. [4] numerically studied the driver gas contamination and the interactions of the reflected shock with the incident boundary layer and the contact surface in tailored conditions. The driver and driven gases of the impulse shock tunnel were He and N_2. The unsteady axisymmetric Navier-Stokes equations for laminar flow were solved by the multiblock finite volume method. A series of computations were conducted to study the wall suction effect on the delay of the driver gas contamination. By using a conical ring to capture the driver gas jet stream, the arrival time in the nozzle was increased by a factor of 2.5 in comparison with the numerical results without the wall suction. Goozée et al. [5] performed a complete reflected shock tunnel simulation with an iris-based model of the primary diaphragm rupture mechanics and the Baldwin-Lomax turbulence model. Two operating conditions, over-tailored and approximate tailored conditions, were examined. In their work, reflected shock/contact surface interactions enhanced the vorticity generation in the over-tailored case. But, in general the flow mechanism was similar for both conditions. Daru and Tenaud [6] worked on the simulation of the viscous shock tube problem by using the monotonicity-preserving scheme. They numerically studied the interaction of reflected shock and boundary layer for Reynolds numbers in the range of 200 to 1000. The working fluid was perfect air and the shock Mach number was 2.37. Two numerical approaches, WENO (Weighted Essentially Non-Oscillatory) space discritization coupled with Runge-Kutta time integration and OSMP (coupled time and space intergration with monotonicity-preserving properties), were compared for validation.

Based on the aforementioned studies, it is found that most previous studies were focused on the single fluid simulations at low Reynolds numbers. Notably, compressible multi-component flow simulations in a shock tube with the real gas effect are barely seen up to date. To achieve (hot) hypersonic flows in a reflected shock tunnel, the real gas effect in the reservoir region of the shock tube end, associated with the high-temperature (high-enthalpy) conditions, is inevitable. Although a number of studies about the reflected shock in shock tube [7-9] have been reported by using experimental or numerical approaches, compressible multi-component flow simulations in connection with the real gas effect remains a challenge for CFD. In this study, a compressible multi-component flow solver is developed in order to deal with the compressible multi-component flow problems. A reduced five-equation model [10-12] is chosen for the simulation of the compressible multi-component flows and HLLC (Harten–Lax-van Leer scheme for Contact surface) approximate Riemann solver [13, 14] is employed to compute numerical flux due to its good performance in high-speed flow, particularly the capability of capturing contact surfaces. For the real gas effect, a curve-fitting approximation for equilibrium air constructed from Grabau-type transition functions [15] is employed. For turbulence model, Baldwin-Lomax turbulence model [16] is adopted. The model is a two-layer algebraic zero-equation model. It has been proved robust for high-speed flows with thin boundary layers [5]. Besides, parallel computation is implemented in the present numerical computations, and MPI is used for information communication between computational nodes.

In this study, several typical test cases are demonstrated first for validation. Subsequently, air-He shock tube simulations with the real gas effect are performed in order to investigate the real gas effect. A simplest schematic diagram of a shock tube with the x-t diagram of the incident shock, the reflected shock, the contact surface, and expansion waves is illustrated in Fig. 1, where the high and low pressure sections are commonly referred to the driver and driven sections of the shock tube, respectively. For air-He shock tube used in this work, the driver and driven gas are He and air respectively. Moreover, the shock bifurcation has been an important issue on driver gas contamination which is a key issue of hypersonic shock tunnel design. Therefore, the shock bifurcation phenomenon for high-speed multi-component flows [1-2, 6, 17] in the shock tube part of a reflected shock tunnel is also simulated in this work. The simulation results of the shock bifurcation are presented to demonstrate the capability of the present numerical approach.
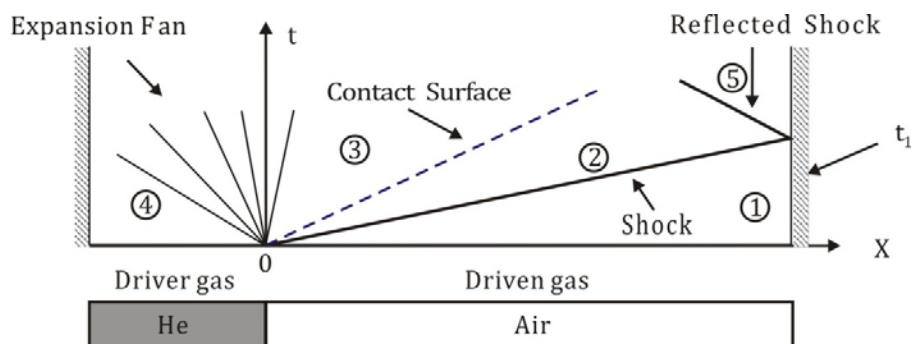

Fig. 1 Schematic x-t diagram of a shock tube

II. Numerical Methods

A. Governing Equation and Reduced Five-Equation Model

This study aims to simulate the reflected shock interacting with the boundary layer in a shock tube. In order to save the computational time, the shock tube flow was assumed to be axisymmetric and only was the upper half tube used in the simulation. The unsteady compressible two-dimensional/axisymmetric Navier-Stokes equations in conjugation with the reduced five-equation model for two-component flow are described in a non-conservative dimensionless form [18] as Eqs. (1) and (2)

$$\frac{\partial \alpha}{\partial t} + U \cdot \nabla \alpha = 0 \tag{1}$$

$$\frac{\partial Q}{\partial t} + \frac{\partial (F - F_v)}{\partial x} + \frac{\partial (G - G_v)}{\partial y} + \Phi H = 0 \tag{2}$$

and

$$Q = \begin{bmatrix} \alpha_1 \rho_1 \\ \alpha_2 \rho_2 \\ \rho u \\ \rho v \\ \rho E \end{bmatrix}, \ F = \begin{bmatrix} \alpha_1 \rho_1 u \\ \alpha_2 \rho_2 u \\ \rho u^2 + p \\ \rho uv \\ (\rho E + p)u \end{bmatrix}, \ G = \begin{bmatrix} \alpha_1 \rho_1 v \\ \alpha_2 \rho_2 v \\ \rho uv \\ \rho v^2 + p \\ (\rho E + p)v \end{bmatrix}, \ H = \frac{1}{y} \begin{bmatrix} \alpha_1 \rho_1 v \\ \alpha_2 \rho_2 v \\ \rho uv \\ \rho v^2 \\ H_5 \end{bmatrix},$$

$$F_v = \begin{bmatrix} 0 \\ 0 \\ \mu(2u_x - \frac{2}{3} \nabla \cdot U) \\ \mu(v_x + u_y) \\ \mu[2uu_x + (u_y + v_x)v - \frac{2}{3}(\nabla \cdot U)u + \frac{\gamma}{\text{Pr}} \frac{\partial}{\partial y}(\frac{p}{\rho(\gamma - 1)})] \end{bmatrix},$$

$$G_v = \begin{bmatrix} 0 \\ 0 \\ \mu(v_x + u_y) \\ \mu(2v_y - \frac{2}{3} \nabla \cdot U) \\ \mu[2vv_y + (u_y + v_x)u - \frac{2}{3}(\nabla \cdot U)v + \frac{\gamma}{\text{Pr}} \frac{\partial}{\partial y}(\frac{p}{\rho(\gamma - 1)})] \end{bmatrix},$$

$$E = \frac{p}{(\gamma - 1)\rho} + \frac{1}{2}(u^2 + v^2),$$

$$H_5 = (\rho E + p)v - \mu[2vv_y + (u_y + v_x)u - \frac{2}{3}(\nabla \cdot U)v + \frac{\gamma}{\text{Pr}}\frac{\partial}{\partial y}(\frac{p}{\rho(\gamma-1)}) \quad ,$$

where α denotes the volume fraction and $\sum \alpha_i = 1$, $U = [u \quad v]$ is the velocity vector, $\Phi = 0$ stands for two-dimensional flow and $\Phi = 1$ for axisymmetric flow, μ is viscosity coefficient, and Pr represents Prandtl Number. The mixture density is given by $\rho = \sum \alpha_i \rho_i$, where the subscript index i ($=1, 2$) denotes the fluid species. α_1 denotes the He volume fraction, so we have air volume fraction, $\alpha_2 = 1-\alpha_1$. $\nabla \cdot U = u_x + v_y + v/y$ for axisymmetric flow. The subscripts x and y of u and v denote partial derivatives.

For Eq. (1), Perigaud and Saurel [18] imposed the condition that the species volume fraction does not to vary across acoustic waves in order to make a model able to realize the coupling across interfaces. Therefore, the diffusion term is neglected to obtain a simplified model which theoretically ensures the positivity of volume fraction α. The detailed information and derivation can be found in the work of Perigaud and Saurel [18].

In this work, the numerical flux is computed by using HLLC approximate Riemann solver, which has been widely used in compressible multiphase flow simulations, especially for flow fields with contact surfaces. For turbulence model, Baldwin-Lomax turbulence model [16] is adopted.

B. Stiffened Equation of State

It is necessary to involve one more equation to close the aforementioned reduced five-equation model. Thus, the stiffened equation of state (EOS) is chosen in this study to fulfill the condition, due to its simplicity for gas and liquid fluids and its excellent numerical stability characteristics on the interface:

$$p = (\gamma-1)\rho e - \gamma\pi, \tag{3}$$

where γ and π are the mixture thermodynamic constant and the mixture reference pressure, respectively [19]. Since the pressure equilibrium between the fluids is assumed in this model, γ and π can be calculated from Eqs. (4) and (5):

$$\frac{1}{\gamma-1} = \sum_i \frac{\alpha_i}{\gamma_i-1} \quad ; \tag{4}$$

$$\frac{\gamma\pi}{\gamma-1} = \sum_i \frac{\alpha_i\gamma_i\pi_i}{\gamma_i-1} \quad . \tag{5}$$

Based on this model, the mixture speed of sound is defined as $c = \sqrt{\gamma(p+\pi)/\rho}$.

Note that stiffened EOS is often used for multi-component flow simulations, especially for liquid and gas mixtures. In general, the reference pressure, π, which represents the molecular attraction between molecules [19], is used for liquid fluids. γ and π are dependent constants which can be determined by a fitting procedure from laboratory data. A typical set of parameter values is for water: $\gamma=7$, $\pi=3000$ atm., and for human blood: $\gamma=5.527$,

π=614.6 MPa, approximately. In this work, both He and air are gases. So, the reference pressure, π, is zero. The stiffened EOS can be reduced to ideal gas EOS. The mixture thermodynamic constant γ becomes the specific heat ratio. The details of calculating γ will be introduced in the next subsection. Basically, the reduced five-equation model proposes a simple concept to simulate the compressible multi-component flow. In this work, we found that it is capable of dealing with the flow fields consisting of strong shocks, shock-shock interactions and shock-interface interactions. It is noted that the present numerical approach has been successfully applied to simulate the shock interaction problems in multi-component flows [20, 21] and good agreements were obtained by comparing with previous numerical and experimental results.

C. Equilibrium Air Model

For hypersonic flows, the gas particle may begin to dissociate or ionize because of the high-temperature effect. Under the high-temperature condition, the thermodynamic properties of gas will differ far from the ideal gas. The effect of dissociation and ionization of the gas to the thermodynamic properties are generally called real gas effects. In heating air, the dissociation and ionization of the gas molecules will start when the temperature is higher than 2000K (dissociation of Oxygen and Nitrogen will take place over 2500 K and 4000K, respectively). According to the work of Feldman [22], the dissociation and recombination relaxation time are very short compared with the time needed for the supersonic flow past the body of certain size. In our shock tube case, the temperature of gas in region 2 is not high enough to cause dissociation and ionization to take place. In the region behind the reflected shock (region 5) where the dissociation and ionization should be considered significantly, the flow velocity is almost static and the gas density is higher than the standard condition which means that the dissociation and recombination relaxation time will be even shorter. Considering the slower flow velocity and shorter relaxation time, the chemical reaction in our cases can be assumed chemical equilibrium.

In order to incorporate the real gas effect, the simplified curve-fitting approximation for equilibrium air constructed from Grabau-type transition functions [15] was used to obtain the thermodynamic properties of air, such as pressure, speed of sound, temperature, enthalpy, density, and internal energy. In the flow calculation of air in thermodynamic equilibrium, it is important to know the various thermodynamic properties as functions of a pair of independent state variables, such as $p = p(e,\rho),\ c = c(e,\rho),\ T = T(e,\rho),\ \gamma = \gamma(e,\rho),$ etc. The fitting curves for thermodynamic properties of equilibrium air exhibit segments of linear or quadratic functions successively connected by transition functions. In this work, the simplified curve fits proposed by Srinivasan et al. [15] for the thermodynamic properties of equilibrium air was adopted. The validated range of the temperature for the fitting curve is up to 25000K and the density ratio is in the range of 10^{-7} to 10^3 (ρ/ρ_o). The thermodynamic properties of air, including γ, were computed directly by using these fitting curves. According to the report of Gordan and McBride [23] for monatomic gases, the gas constant γ of He approximates a constant (=1.67) in the test range of temperature. Hence, it is reasonable to use perfect gas EOS for He in the present simulations. As mentioned in Section II-B, for the mixture of He and air, the stiffened equation of state (4) is used to calculate the mixture gas constant γ.

III. Results

A. Shock Tube Problem

One important purpose of this study is to investigate the real gas effect in hypersonic multi-component flows. In this subsection, several test cases of air-He shock tube problems were conducted to validate the current equilibrium air model, by comparing the obtained results with the ideal gas and CEA (chemical equilibrium with applications) [24] solutions. When using the ideal gas model, air was considered with constant specific heat ratio (γ=1.4) and constant fluid properties at room temperature of 300 °K in our code. CEA software, which has been well validated experimentally in the literature, may serve to provide reference solutions for the comparison purpose [25]. Notably, the shock function in CEA performs a 1-D inviscid calculation of equilibrium air properties behind the incident and reflected shocks. Therefore, the inviscid form of Eq. (2) was adopted as the governing equation in this subsection for comparison, by neglecting the dissipation terms.

The shock tube with both length and diameter of 1m was considered in this study. To check the robustness of the code and understand the fundamental problems in the shock tube, including the reflected shock/turbulent boundary layer interactions in the following subsection, we imposed the axisymmetric assumption in the first place. Note that, in the real shock tube/tunnel operation, three dimensional effects are inevitable, with the diaphragm(s) opened non-axisymmetrically. The computational domain covers only half the shock tube (1m × 0.5m) because of the axisymmetric flow assumption. The mesh of the grid consists of 100 × 50 cells for the inviscid tests in this subsection. Initially the diaphragm is located at x = 0.5m. For wall boundary conditions, all boundaries are adiabatic walls. Furthermore, to save the computing time, the parallel computation was performed with MPI by using 16 CPUs. The simulation parameters are listed in Table 1. The initial driver and driven gas temperatures were set to room temperatures (300K) for all test cases. For working fluids, He and air were chosen as the driver gas and the driven gas, respectively. The Reynolds numbers were estimated by the flow properties behind the incident shock obtained from the present numerical simulation. The reference length scale is 1m (i.e., the diameter of the shock tube). Due to the real gas effect, the air properties differ from the ideal gas resulting in the differences of Reynolds numbers.

Figure 2 presents the incident shock Mach numbers varies with different diaphragm pressure ratios ($P_{41} \equiv P_4/P_1$). It is found that the cases with the equilibrium air model have lower incident shock Mach numbers in comparison with the cases with the ideal gas model. Besides, the differences of incident Mach numbers between the ideal gas model and the equilibrium air model become relatively larger when the diaphragm pressure ratio increases, indicating the real gas effect becomes more important with higher diaphragm pressure ratios.

Table 1 Parameters of Air-He Shock Tube Simulations

Case	p_1 (atm.)	p_4 (atm.)	Shock Mach Number	Reynolds Number	EOS
1	1	76	3.40	1.05×10^8	Ideal gas
2	1	76	3.39	1.13×10^8	Equilibrium air model
3	1	100	3.61	1.11×10^8	Ideal gas
4	1	100	3.58	1.20×10^8	Equilibrium air model
5	1	150	3.92	1.18×10^8	Ideal gas
6	1	150	3.87	1.33×10^8	Equilibrium air model
7	0.3	150	4.86	3.98×10^7	Ideal gas
8	0.3	150	4.80	4.67×10^7	Equilibrium air model
9	0.2	150	5.21	2.73×10^7	Ideal gas
10	0.2	150	5.11	3.26×10^7	Equilibrium air model
11	0.1	150	5.75	1.40×10^7	Ideal gas
12	0.1	150	5.62	1.78×10^7	Equilibrium air model
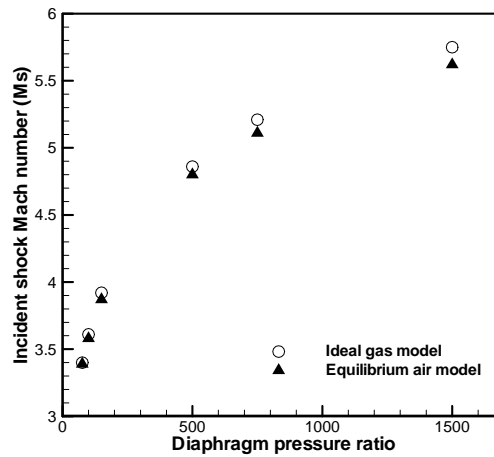
Fig. 2 Comparison of incident shock Mach numbers varying with different initial pressure ratios P_{41}

Figure 3 presents the comparisons of pressures behind the incident (P_2) and reflected (P_5) shocks varying with different diaphragm pressure ratios among the ideal gas model, the equilibrium air model and CEA (chemical equilibrium with applications) solutions. It can be seen that only slight differences among different models for both pressures behind the incident and reflected shocks. Notably, the present results with the equilibrium air model are in good agreements with CEA results. The differences between simulation results with the equilibrium air model and CEA results of P_2 and P_5 are less than 1% and 5% at the diaphragm pressure ratio of 1500.   Figure 4 shows the

comparisons of temperatures behind the incident and reflected shocks varying with different diaphragm pressure ratios among the ideal gas model, the real gas model and CEA solutions. As shown in Fig. 4, it obviously demonstrates that real gas effect shows a significant influence on temperature, especially for strong shock Mach numbers. Again, it is found that the present results with the equilibrium air model are in excellent agreements with CEA results. In addition, the difference of the temperature obtained from the present results between the ideal gas model and the equilibrium air model are found approximately up to 1350K as the diaphragm pressure ratio up to 1500. Consequently, from the results of Figs. 3 and 4, the importance of the real gas effect for hypersonic shock tunnel flows is shown. Through the present shock tube tests, the accuracy of the present equilibrium air model is also exhibited.

(a)   (b)
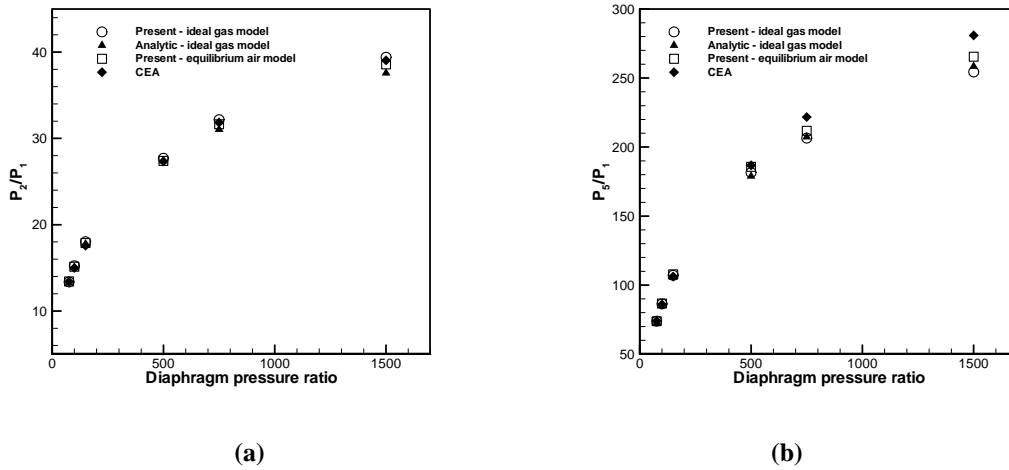
Fig. 3 Comparisons of the variations in pressure ratios (a) P_2/P_1 and (b) P_5/P_1 with different diaphragm pressure ratios among the ideal gas model, the equilibrium air model and CEA solutions.

(a)   (b)
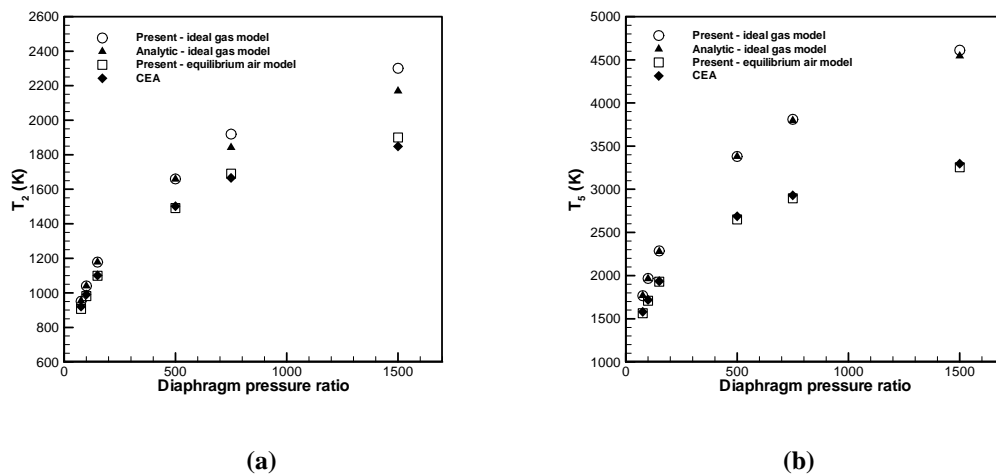
**Fig. 4 Comparisons of the variations in (a) temperature behind the incident shock (T_2) and (b) temperature**

behind the reflected shock (T_5) with different diaphragm pressure ratios among the ideal gas model, the equilibrium air model and CEA solutions.

B. Reflected Shock/Boundary Layer Interaction Problems

In order to understand the grid effect on the reflected shock/boundary layer interaction problem, four grid sizes of 1000×500, 2000×1000, 2500×1250, and 3000×1500 cells, were used for the grid test by using the present multi-component axisymmetric compressible Navier-Stokes flow solver with the equilibrium air model and the Baldwin-Lomax turbulence model. Notably, the mesh distribution is uniform in x-direction, but non-uniform in y-direction. The computational domain is the same as that of the shock tube problem in the previous subsection. The diaphragm is initially located at x = 0.5 m, and all boundary conditions are no-slip walls. For initial conditions, cases 4 and 8 in Table 1 were chosen. In all tests, air and He were chosen as driven and driver gases, respectively. The x-t diagrams of shock front and contact surface for cases 4 and 8 are shown in Figs. 5(a) and 5(b), respectively. It is found that both results of shock front and contact surface for 4 different grids are within acceptable accuracy. In Fig. 5(c), the pressure profiles along y-axis at x= 0.86 m and t=0.00065 s for case 4, obtained by using these 4 different grids, are presented. The upper wall is located at y=0.5 m. The differences due to the increased resolution in the separate flow layer from the fine-grid solutions are clearly seen. Consequently, the grid size of 2500×1250 grid points is adopted in this study. Note that at t=0.00065, the reflected shock has not reached x= 0.86 m, while the bifurcation foot and the separation bubble are passing by (see later descriptions of Fig. 8).
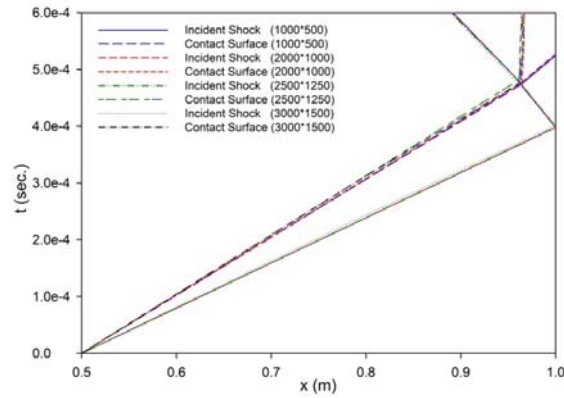
(a)
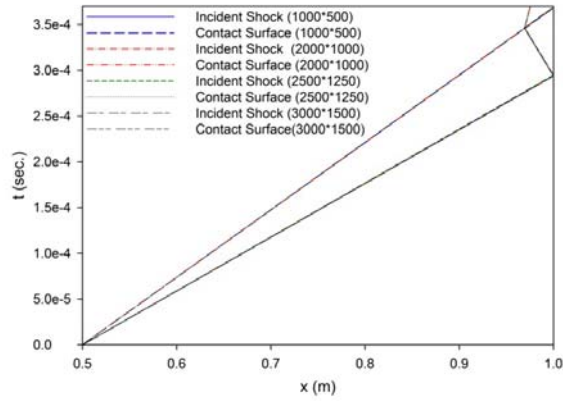
(b)
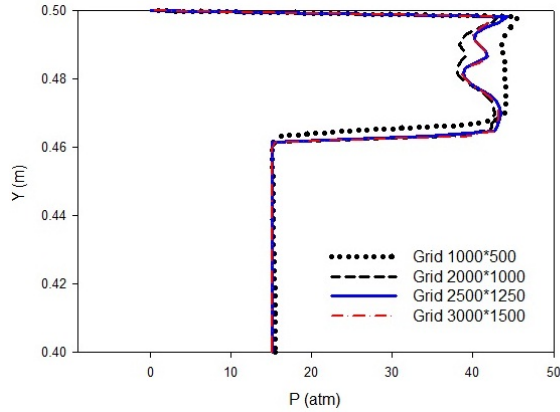
(c)

Fig. 5 Grid test for 4 different grid sizes: (a) and (b) are the comparisons of the shock front and contact surface trajectories in the *x*-t diagram for case 4 and case 8, respectively, and (c) is comparison of pressure profiles along *y* direction at *x*= 0.86m and t=0.00065 s for case 4.

For shock/ turbulent boundary layer interaction problems, the effect of the turbulent boundary layer on the separation distance between incident shock and contact surface is an important issue. It is known that in an ideal inviscid shock tube, the separation distance increases linearly with distance from the diaphragm. However, in a real shock tube, the wall boundary layer between the shock and contact surface acts an aerodynamic sink and absorbs mass from this region, consequently causing the contact surface to accelerate and the shock to decelerate. The separation distance ι is reduced below the ideal value. The separation distance approaches a limiting (maximum) value ι_m. Figure 6 presents a quantitative comparison of separation distance as a function of the distance from diaphragm. The non-dimensional variables ζ and η are defined as $\zeta = \iota/\iota_m$ and $\eta = x_s/W\iota_m$, where x_s is the

shock distance from the diaphragm, the non-dimensional variable $W = u_s/(u_s - u_2)$, and the subscript s and 2 denote the states of shock and the flow behind the shock, respectively [26]. It is found that the present results agree well with the analytical solutions of Mirels [26]. Therefore, the present numerical method is proved to be capable of dealing with the shock tube flows with shock/ turbulent boundary layer interactions.

In order to understand the flow mechanisms of boundary layer/reflected shock interactions, the cases listed in Table 1 were selected for numerical simulation. The duration between incident shock reflected from the end wall and then interacting with the expansion wave tail was adopted to observe the shock bifurcation phenomena in order to minimize the interference generated by the shock/expansion wave interactions. In Fig. 7, the typical shock bifurcation structures consisting of the reflected shock wave, slip line, tail shock, bifurcation foot, and separated bubble are revealed with the magnified computed Schlieren image (of Fig. 8(e)), where the corresponding incident shock Mach number is 3.87 (case 6 in Table 1) and the equilibrium air model is considered.
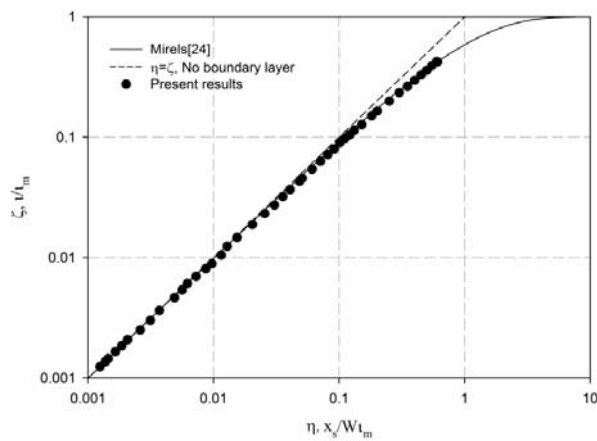

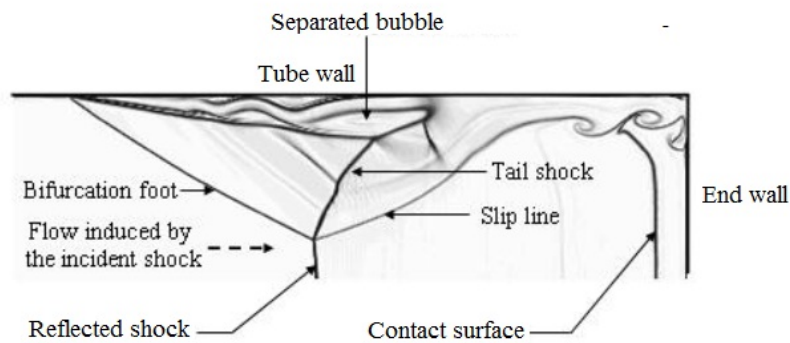**Fig. 6 Comparison of separation distance as a function of distance from diaphragm**

Fig. 7 Magnified computed Schlieren image showing shock bifurcation structures for the case of Ms=3.87

Figure 8 shows a series of computed Schlieren images during the shock bifurcation development for the case of Ms=3.87. In Fig. 8(a), the incident shock has just reflected from the end wall and started to interact with the boundary layer. At the beginning, the adverse pressure gradient caused by the reflected shock separates the boundary layer induced by the incident shock and yields a separated bubble. A lambda-like shock forms. In Fig. 8(b), the reflected shock propagates upstream and the separation bubble continues to grow. At this stage, the typical flow structures of shock bifurcation containing the bifurcated foot, slip line and separated bubble are clearly observed. As shown in Fig. 8(c), the reflected shock continues to propagate upstream. The profile of shock bifurcation keeps growing; meanwhile, maintains similar structures. It is also observed that the slip line starts to become unstable due to the shearing force between the separated flow and the lower wall. In Fig. 8(d), the shear-layer instabilities are enhanced while the reflected shock is continuing to move upstream. The slip line eventually rolls up to form vortices. In Fig. 8(e), basically the flow structures of shock bifurcation have fully developed. The evolution of these complex unsteady flow structures is similar to that observed by Daru and Tenaud [6].The present numerical methods are found capable of dealing with the simulation of shock bifurcation in the shock tube of a reflected shock tunnel for hypersonic researches.

Shock bifurcation is highly related to the driver gas contamination problem occurring in shock tunnels [4, 5]. In order to study the detailed mechanism of the driver gas contamination problem, the contours of temperature and species volume fraction for case 6 in Table 1 (Ms=3.87 with equilibrium air model) are presented in Fig. 9. Figures 9(a)− 9(d) present the contours of air volume fraction at different instants. In Fig. 9(a), the driver gas begins to be enrolled into the driven gas due to the boundary layer separation. In Fig. 9(b), the recirculating driver gas has impinged the top wall surface resulting in driven gas separation into two regions. In Fig. 9(c), the recirculating driver gas forms a high-speed jet in the separated boundary layer and a small amount of the driver gas moves toward the end wall leading to the driver gas contamination. In Fig. 9(d), the driver gas contamination proceeds with the development of shock bifurcation. Figures 9(e)− 9(h) present temperature contours at instants corresponding to Figs. 9(a)− 9(d). As seen, in contrast to the driver gas, the driven gas flow is rather hot. During the shock bifurcation, the cold driver gas is drawn into the hot separation region. It is also found that the high-speed cold jet penetrates into the hot separated boundary layer. Furthermore, the velocity vectors and vorticity contours of the flow at t=0.0006s in Fig. 9(d) is shown in Fig. 10. It is observed that the strong vorticity appears in the vicinity of the separation region. The driver gas contamination process observed by the present simulations is essentially conformable to the previous results of Daru and Tenaud [6], although their Reynolds numbers were only in the range of 200 to 1000. The present numerical approach successfully simulated the temperature and species concentration contours during the reflected shock/turbulent boundary layer interaction in the shock tube to better understand the driver gas contamination problem.

Figure 11 shows the comparison of triple point trajectories between the ideal gas and equilibrium air models, where X stands for the distance of triple point to the end wall and Y for the height of triple point. The time interval

between two adjacent data points is 50 μs for all cases. As shown in Fig. 11, both X and Y for the ideal gas model are larger than those for the equilibrium air model at the same instant. Notably, the shock Mach numbers for the equilibrium air model are slightly smaller than those for the ideal gas model. Therefore, the development of shock bifurcation for the ideal gas model is faster than for the equilibrium model. In addition, it is found that the trajectory of triple point shows a near-linear growth rate and the larger M_s is, the larger the growth rate of Y is. These two observations are consistent with those in the literature [2, 3].

Table 2 shows the real gas effect on the bifurcation foot angle $\emptyset$ and the deflection angle θ for different diaphragm pressure ratios, where the bifurcation angle $\emptyset$ denotes the angle between the front leg of bifurcation and the wall surface and the deflection angle θ denotes the angle between the oblique shock and the wall surface. A schematic diagram of shock bifurcation showing the bifurcation foot angle $\emptyset$ and the deflection angle θ is illustrated in Fig. 12. In the present numerical simulations, the predicted bifurcation foot angle $\emptyset$ is nearly a constant after the shock bifurcation is fully developed. This result agrees with the experimental observation of Matsuo et al. [2]. Besides, the present numerical simulations predict that deflection angle θ is also nearly a constant. As listed in Table 2, high initial pressure ratio results in small bifurcation angle $\emptyset$ and deflection angle θ. This phenomenon again agrees with the theoretical predictions of Mark [1] and Matsuo et al. [2]. Furthermore, the bifurcation angle $\emptyset$ and the deflection angle θ simulated by using the ideal gas model are smaller than those simulated by using equilibrium air model. The effect of the real gas effect on the development of shock bifurcation is demonstrated.

IV. Conclusions

In this study, a compressible multi-component Navier-Stokes flow solver was developed to simulate the Air-He shock tube problem, using a reduced five-equation model in conjunction with HLLC approximate Riemann solver. The equilibrium air model of Srinivasan et al. [15] and the Baldwin-Lomax turbulence model were also included to consider the real gas effect and the reflected shock/turbulent boundary layer interaction. The present simulation results of the temperature and pressure behind the incident and reflected shocks with the equilibrium air model are in good agreement with the CEA results. The significance of the real gas effect on the temperature behind the incident and reflected shocks and the profiles of shock bifurcation structures during the reflected shock/turbulent boundary layer interactions were clearly demonstrated. The temperature difference between the real gas model and the ideal gas model is about 1350 °K when the diaphragm pressure ratio is 1500. The ideal gas model over-predicted the temperature significantly. The development of the shock bifurcation phenomena, which is highly related to the driver gas contamination problem in the shock tunnel operation, were also clearly presented with the computed Schlieren images and the numerical contours of temperature and species volume fraction. It is shown that the development of shock bifurcation for the ideal gas model is faster than for the equilibrium model. The trajectory of triple point exhibits a near-linear growth rate and the larger the shock Mach number is, the larger the growth rate of

the height of triple point is. This study shows the feasibility of using the present numerical approach in the high-speed multi-component flow simulations and in the design of a high-enthalpy shock tunnel. Follow-on studies should include the influence of three-dimensional effects, which may play an important role in the instabilities observed in the shear layer. This is especially important for the axisymmetric circular shock tube in the real application, having a radius on the order of magnitude as the bifurcation height.
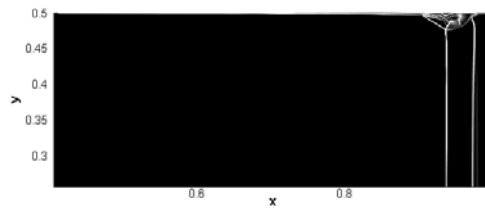
(a) t=0.0005s
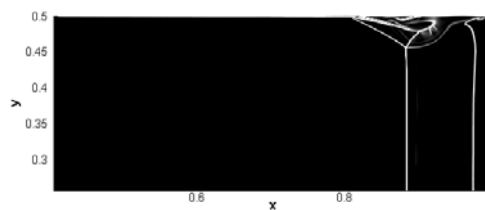
(b) t=0.0006s
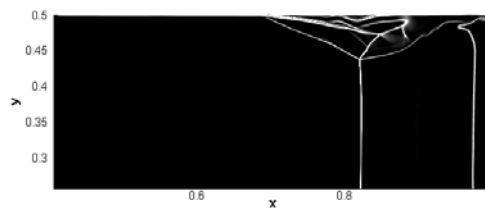
(c) t=0.0007s
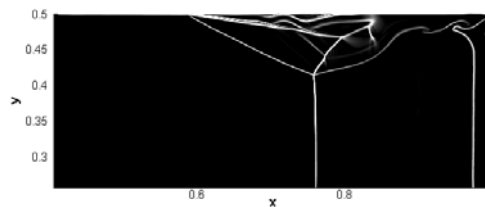
(d) t=0.0008s
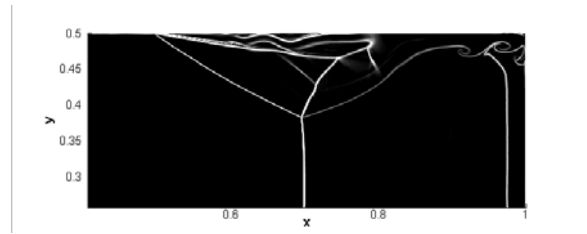
(e) t=0.0009s

Fig. 8 Computed Schlieren images of shock bifurcation development for the case of Ms=3.87

(a) t=0.00045s   (e) t=0.00045s

(b) t=0.0005s   (f) t=0.0005s

(c) t=0.00055s   (g) t=0.00055s
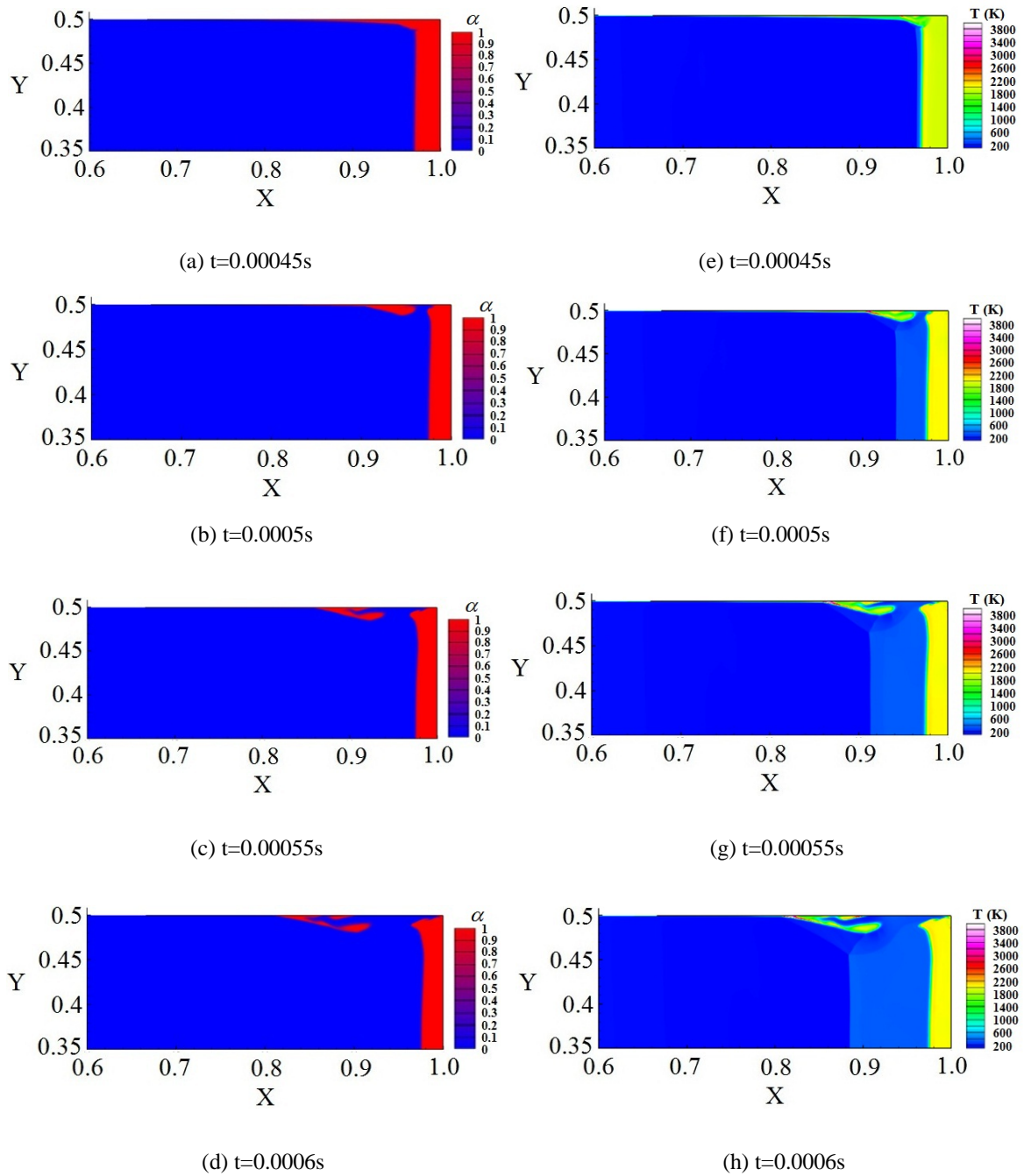
(d) t=0.0006s   (h) t=0.0006s

Fig. 9 Contours of species volume fraction and temperature for case 6 in Table 1 (Ms=3.87 with equilibrium air model) at different instants of shock bifurcation. (a)−(d): air volume fraction; (e)−(h): temperature.
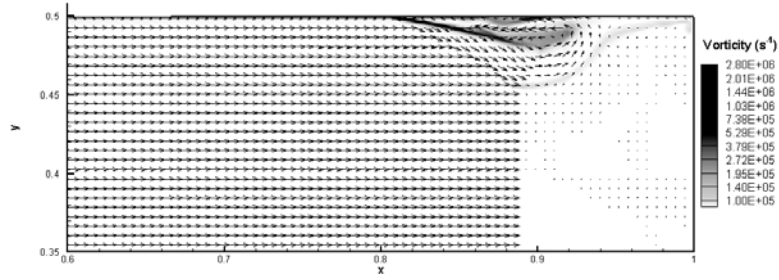
Fig. 10 Velocity vectors and vorticity contours for case 6 in Table 1 (Ms=3.87 with equilibrium air model) at t=0.0006s.
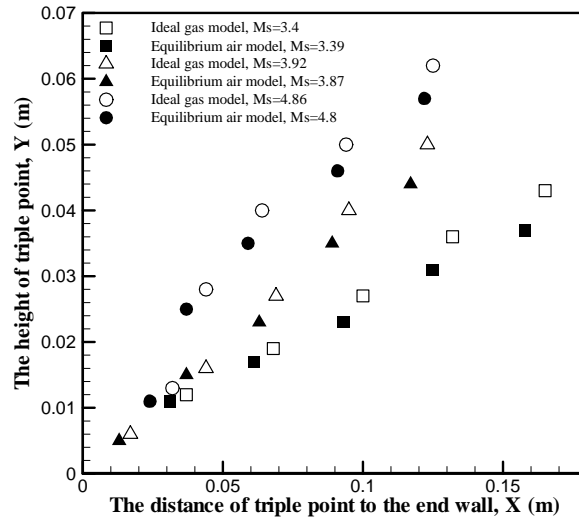

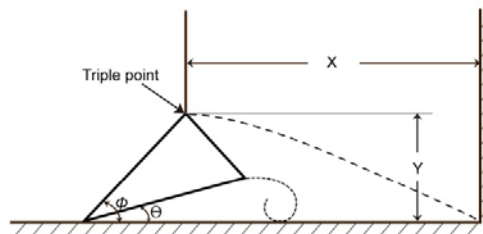**Fig. 11 Comparison of triple point trajectories for different models**

Fig. 12 Schematic diagram for shock bifurcation

Table 2 Real gas effect on the bifurcation foot angle $\emptyset$ and the deflection angle θ for different initial diaphragm pressure ratios

	Equilibrium air model		Ideal gas model	
P_{41}	76	150	76	150
$\emptyset$ (deg.)	33	27	32	26
θ (deg.)	13.5	12	11	9.5

Acknowledgments

References

[1] Mark, H., "The Interaction of a Reflected Shock Wave with the Boundary Layer in a Shock Tube," NACA-TM-1418, 1958

[2] Matsuo, K., Kawagoe, S. and Kage, K. "The Interaction of a Reflected Shock Wave with the Boundary Layer in a Shock Tube," *Bulletin of the JSME*, Vol. 17, No. 110, 1974, pp. 1039-1046

[3] Weber, Y. S., Oran, E. S., Boris, J. P. and Anderson, J. D. Jr., "The Numerical Simulation of Shock Bifurcation near the End Wall of a Shock Tube," *Physics of Fluids*, Vol. 7, 1995, pp. 2475-2488

[4] Burtschell, Y., Cardoso, M. and Zeitoun, D. E., "Numerical Analysis of Reducing Driver Gas Contamination in Impulse Shock Tunnels," *AIAA Journal*, Vol. 39, No. 12, 2001, pp. 2357-2365

[5] Goozée, R. J., Jacobs, P. A. and Buttsworth, D. R., "Simulation of a Complete Reflected Shock Tunnel Showing a Vortex Mechanism for Flow Contamination," *Shock Waves*, Vol. 15, 2006, pp. 165-176

[6] Daru, V. and Tenaud, C., "Numerical Simulation of the Viscous Shock Tube Problem by Using a High Resolution Monotonicity-Preserving Scheme," *Computers & Fluids*, Vol. 38, 2009, pp. 664-676

[7] Holder, D. W., Schultz, D. L., "On the Flow in a Reflected Shock Tunnel," A. R. C. R&M NO.3265, 1962.

[8] Pennelegion, L., Gough, P. J., "The Change in Shock-Tunnel Tailoring Mach Number Due to Driver Gas Mixtures of Helium and Nitrogen ," A. R. C. R&M NO.3398, 1965.

[9] Gaydon, A. G., Hurle, L. R., "The Shock Tube in High Temperature Chemical Physics," Reinhold Publishing Corporation, 1963.

[10]   Shyue, K. M., "A Fluid-Mixture Type Algorithm for Barotropic Twofluid Flow Problems," *Journal of Computational Physics,* Vol. 200, 2004. , pp.718-748

[11]   Saurel, R., LeMetayer, O., "A Multiphase Model for Compressible Flows with Interfaces, Shocks, Detonation Waves and Cavitation," *Journal of Fluid Mechanics*, Vol. 431, 2001. , pp. 239-271

[12]   Allaire, G., Clerc, S. and Kokh, S., "A Five-Equation Model for Simulation of Interfaces between Compressible Fluids," *Journal of Computational Physics*, Vol. 181, 2002. , pp.577-616

[13]   Harten, A., Lax, P. D. and B. van Leer, "On Upstream Differencing and Godunov-Type Schemes for Hyperbolic Conservation Laws," *SIAM Review*, Vol. 25, 1983. , pp. 35-61

[14]   Toro, E. F., Spruce, M., and Spears, W., "Restoration of the Contact Surface in the HLL-Riemann Solver," *Shock Waves*, Vol. 4, 1994, pp. 25-34

[15]   Srinivasan, S., Tanehill, J. C. and Weilmuenster, K. J., "Simplified Curve Fits for the Thermodynamic Properties of Equilibrium Air," NASA RP-1181, 1987.

[16]   Baldwin, B. S. and Lomax, H, "Thin Layer Approximation and Algebraic Model for Separated Turbulent Flows," *AIAA Paper*, 1978, pp. 78-257

[17]   Petersen, E. L. and Hanson, R. K., "Measurement of Reflected-Shock Bifurcation over a Wide Range of Gas Composition and Pressure," *Shock Waves*, Vol. 15, 2006, pp. 333-340

[18]   Jorgenson, P.C.E., Loh, C.Y., "Computing Axisymmetric Jet Screech Tones Using Unstructured Grids ," NASA/TM—2002-211799, AIAA–2002–3889, 2002

[19]   Shyue, K. M., "A Fluid-Mixture Type Algorithm for Compressible Multi component Flow with van der Waals Equation of State," Journal of Computational Physics, Vol. 156, 1999, pp. 43-88

[20]   Chen, H., "Two-Dimensional Simulation of Stripping Breakup of a Water Droplet," *AIAA Journal*, Vol. 46, No. 5, 2008, pp. 1135-1143

[21]   Chen, H., Liang, S. M., "Flow Visualization of Shock/Water Column Interactions," *Shock Waves*, Vol. 17, No. 5, 2008, pp. 309-321

[22]   Feldman, S., "Some Shock Tube Experiments on the Chemical Kinetics of Air at High Temperatures," *Journal of Fluid Mechanics*, Vol. 3, Issue 3, 1957, pp. 225-242

[23]   Gordon, S., McBride, B. J., "Thermodynamic Data to 20000 K for Monatomic Gases," NASA TP-1999-208523, 1999

[24]   NASA Chemical Equilibrium with Applications (CEA), http://www.grc.nasa.gov/WWW/CEAWeb

[25]   Mundt, C., Boyce, R., Jacobs, P. Hannemann, K., "Validation Study of Numerical Simulations by Comparison to Measurements in Piston-Driven Shock-Tunnels," *Aerospace Science and Technology*, Vol. 1, 2007, pp. 100-109

[26]   Mirels, H., "Shock Tube Test Time Limitation Due to Turbulent-Wall Boundary Layer," *AIAA Journal*, Vol. 2, No. 1, 1964, pp. 84-93